



Numerical study on compressive behavior of a 3D-printed sand mold-cast S-CN connector

Tran-Van Han^{a,d}, Jeong MoonSook^b, YongNam Kim^c, Dongkyu Lee^a, Nguyen-Vu Luat^e, Kihak Lee^{a,*}

^a Deep Learning Architecture Research Center, Department of Architectural Engineering, Sejong University, 209 Neungdong-ro, Gwangjin-gu, Seoul 05006, Republic of Korea

^b Samsung C&T Corp., 26 Sangil-ro 6-gil, Gangdong-gu Seoul, Seoul 05288, Republic of Korea

^c Mirae Structural Engineering Co., Ltd., 417 Daemyung Bellion, 127 Beobwon-ro, Songpa-gu, Seoul, Republic of Korea

^d Faculty of Civil Engineering, Mien Trung University of Civil Engineering, Tuy Hoa and Danang, Viet Nam

^e MIT University Vietnam, Highway No. 1A, Dau Giay, Thong Nhat, Dong Nai 76000, Viet Nam

ARTICLE INFO

Keywords:

Modular construction
3D sand printing
Rectangular hollow section
modular connection
Finite element analysis

ABSTRACT

This paper presents a novel approach for steel modular structures, incorporating the S-CN connector – a hybrid tie rod and connector connection method – along with rectangular hollow section (RHS) steel members. The study numerically investigates the mechanical behavior of S-CN connectors and their application in beam–column connections under compressive loading. The compressive load-bearing capacity of the proposed connection is determined following AISC 360-16 guidelines, predicted through a finite element analysis approach and validated by experimental data. Parametric analysis reveals the impact of local buckling in modular nodes on the connector's load-bearing capacity. The results demonstrate that tie plate thickness has a minimal effect, while reducing the modular node thickness leads to a linear decrease in load capacities. Furthermore, the failure mode of the beam–column connection depends on the compressive capacities of both the RHS column and the S-CN connector.

1. Introduction

The construction industry has been witnessing a paradigm shift with the increasing adoption of modular construction, a type of pre-fabricated building technique that utilizes volumetric and panelized systems [1]. This innovative approach involves the offsite fabrication of entire building modules, such as complete rooms or sections, in a controlled factory environment. These modules are then transported to the construction site for assembly, leading to faster construction times, cost savings, improved quality control, and reduced environmental impact [2–9].

Modular construction is considered a promising solution to address various challenges in the construction industry, including the pressing issue of affordable housing shortages [10]. By offering efficient and streamlined construction processes, modular construction has the potential to significantly increase housing supply while keeping costs at a minimum. This has sparked interest in utilizing modular construction for high-rise buildings, which are especially prevalent in urban environments.

One critical aspect of modular construction is the inter-module joining techniques that connect individual modules to form a coherent

building system [11]. These joining techniques play a vital role in ensuring the overall structural integrity, stability, and robustness of the modular building. In high-rise modular buildings, where repeated modules are stacked to achieve height, the importance of reliable and strong connections becomes even more pronounced. However, the lack of effective inter-module joining techniques has been identified as one of the key technical challenges hindering the widespread adoption of modular construction for high-rise buildings [12,13].

To address this challenge, researchers have been exploring and developing various inter-module joining techniques, which can be broadly classified into three groups: (i) tie rod connections, (ii) bolt connections, and (iii) connector-based connections [1]. For (i) the inter-module connection types that use tie rod technique, one noteworthy approach proposed by Chen et al. [14] is the pre-stressed modular connection. This technique involves utilizing pre-stressed strands to join the modular columns vertically. The study demonstrated that this connection imparts considerable stiffness to the modular frame, rendering it robust enough to withstand earthquakes at fortified intensity shake levels. Another innovative method, introduced by Sanches et al. [15],

* Corresponding author.

E-mail address: kihaklee@sejong.ac.kr (K. Lee).

utilizes vertical post-tensioned connections for modular steel structures. This system incorporates a post-tensioned threaded rod and a steel box with conical ends. The results of quasi-static cyclic loading tests showcased the potential benefits of reduced module assembly welding and enhanced lateral resistance. The work of Liew et al. [16] explored a different approach using a gusset plate and rebar to connect adjacent modules horizontally and vertically, facilitating connections between lower and upper modules. Meanwhile, Lacey et al. [17] proposed a new post-tensioned vertical inter-module connection for modular steel buildings, which exhibited excellent initial stiffness in shear, thanks to parameter preloading and slip factor regulation. Additionally, a modular unit connection system, proposed by Farnsworth [18], involved coupled threaded tension rods and a transfer plate with geometric forms aiding module assembly alignment.

The inter-module bolt connections (ii) has also seen significant exploration by various researchers. Deng et al. [19] introduced a bolted connection with a welded cover plate for square hollow section columns. The study conducted seven full-scale T-shape connection tests under monotonic and cyclic loading conditions, providing valuable insights into the behavior of this bolted connection. An innovative modular steel building connection design, proposed by Chen et al. [20,21], utilized an intermediate plug-in device and a beam-to-beam bolt system for horizontal and vertical connections, respectively. Meanwhile, Cho et al. [22] developed the Blind-Bolted connection, utilizing multiple blind and high-tension bolts to effectively connect modules. Other notable contributions include the work of Yu and Chen [3], presenting a connection type with single connecting bolts and an intermediate plate. Lacey et al. [23] introduced an interlocking inter-module connection that combines structural bolts with interlocking elements. This arrangement offers increased initial shear stiffness compared to existing inter-module connection details. Additionally, the modular joint with connection plates proposed by Lee et al. [24,25] demonstrated favorable structural performance when compared to a welded joint reference model, as verified through rigorous testing. Researchers like Sendanayake et al. [26,27] contributed valuable insights by proposing inter-modular connections utilizing bolts, connection plates, and resilient layers, displaying superior dynamic behavior under monotonic and cyclic lateral loads. Furthermore, Sharafi et al. [28] introduced an interlocking system with wide applicability in modular construction projects.

In modular construction, connector-based inter-module connection techniques (iii) have emerged as a superior alternative to traditional rod systems, owing to their simplicity and adaptability [1]. These innovative connectors play a pivotal role in streamlining the assembly process, as they can be pre-welded to columns and beams in factories, facilitating swift and efficient on-site connections of modules. Dhanapal et al. [29] introduced a modern VectorBloc connection that utilized modern cast-steel connectors and hollow structural components. The behavior of Beam-Column Connections and registration pin connection of this type of connector were also studied [30,31]. Addressing specific challenges, Doh et al. [32] conducted research focusing on steel bracket connections. Their work explored innovative methods for achieving secure and efficient connections between modular components, providing valuable insights into the use of steel brackets as connectors. A focus on installation convenience and on-site ornamentation led to the study by Chen et al. [33], which investigated the rotational rigidity of rotary joints in modular structural systems. The findings demonstrated that such connectors offer seamless integration and do not compromise the aesthetics of on-site construction, providing great installation convenience, employing experimental and theoretical techniques. Dai et al. [34] introduced novel connections known as plug-in self-lock joints that not only provided sufficient capacity but were also convenient for on-site construction. An innovative and fully prefabricated liftable connection, utilizing standard corner fittings and long stay bolts, was presented by Deng et al. [35]. The novelty of this connection is that it is easy to hoist the module unit during installation using the corner fitting.

Within this context, Han et al. recently proposed and experimentally tested a novel 3D-printed sand mold-cast S-CN connector, a hybrid of tie rod and connector connection methods, along with rectangular hollow section (RHS) steel members for steel modular structures targeted for Design for Manufacturing and Assembly (DfMA) methodology. The proposed connection using S-CN connector and RHS members has an optimized configuration that is advantageous for large-scale manufacturing (for Design for Manufacture and Assembly DfMA) in an industrial setting. Experimental investigations were performed to assess performance of the connector and its application in corner connections under axial compression loads. The findings highlight the impact of local buckling of the modular nodes on the ultimate load-bearing capacity of the S-CN connector and the corner connection. However, the parameters investigated in the experimental campaign were limited. Thus, further research and additional information are still required for deeper understanding the behavior of this novel connector under several loading conditions. Also, it is of importance to investigate the influence of several parameters over the response of the S-CN connector and beam-column connection using S-CN connector, toward the objectives of obtaining the optimal design condition. These considerations motivated the present research activity, whose main objectives are: (i) to provide insights into the mechanical behavior of S-CN connector under compressive loading; (ii) to propose a method for evaluating the compressive load-bearing capacity of a S-CN connector based on AISC 360–16 standard; (iii) to identify the parameters that mainly affect the local behavior of S-CN connector in view of obtaining specific performance objectives.

To fulfill these objectives, detailed Finite Element (FE) models were developed in ANSYS [36] and validated against the available experimental results of the previously tested S-CN connector specimens. A parametric FE analysis was also conducted on different geometrical configurations to deeper understand the failure mechanism and compressive behavior of the novel S-CN connection. The combination of Finite Element Analysis (FEA) and experimental testing produces more meaningful results and aids in designing future laboratory testing more effectively [37].

The paper is organized as follows: Section 2 presents the concept of the S-CN connector. Section 3 reviews an experimental study of an S-CN connector, outlines the FE modeling strategy, and validates it against experimental results. In Section 4, a procedure is presented to apply the AISC 360–16 standard for evaluating the load-bearing capacity of the S-CN connector. Furthermore, Section 5 describes the investigation of 24 configurations for the S-CN connector and S-CN beam-column connection, and critically compares the results obtained from the parametric FE analysis.

2. The S-CN connector concept

2.1. S-CN modular construction

The utilization of rectangular hollow steel (RHS) for structural components in steel constructions is favored due to its remarkable compression, torsion, and bending characteristics, coupled with an advantageous strength-to-weight ratio [38]. In modular steel construction, there is limited research on inter-module connections using RHS members. Fig. 1 presents several studies that have delved into inter-module connections for steel modular construction employing RHS members. As shown in Fig. 1, Deng et al. [19] proposed a bolted connection with welded cover plate. Chen et al. [20] introduced cast plug-in devices for horizontal connections and high tensile strength bolting for vertical ones. However, these bolted connections, due to their strict installation requirements on the installation accuracy and require opening holes in beams or columns, pose potential architectural concerns [39]. Dhanapal et al. [29] presented modules connected via VectorBloc connectors.

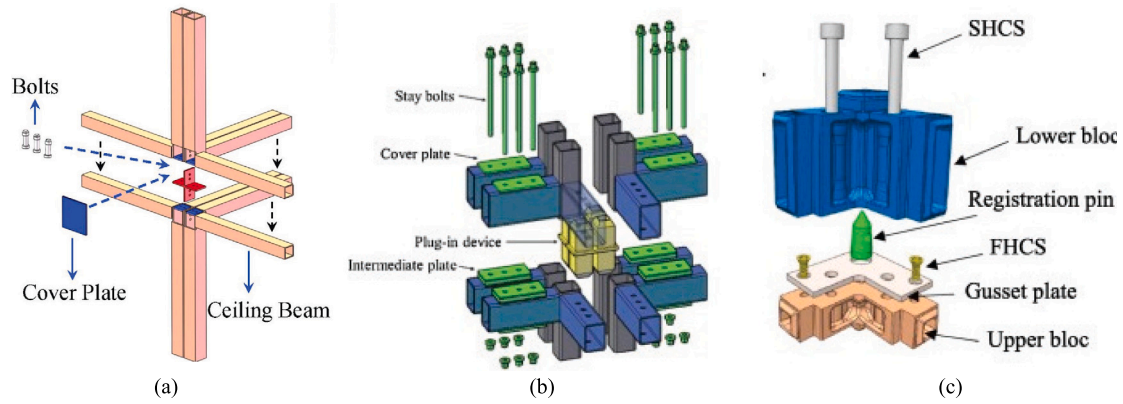


Fig. 1. Representative inter-module connections for steel modular construction using RHS members: (a) Bolted connection with welded cover plate [19] ; (b) Beam - to - beam bolted connection [20] ; (c) VectorBloc modular connector [29].

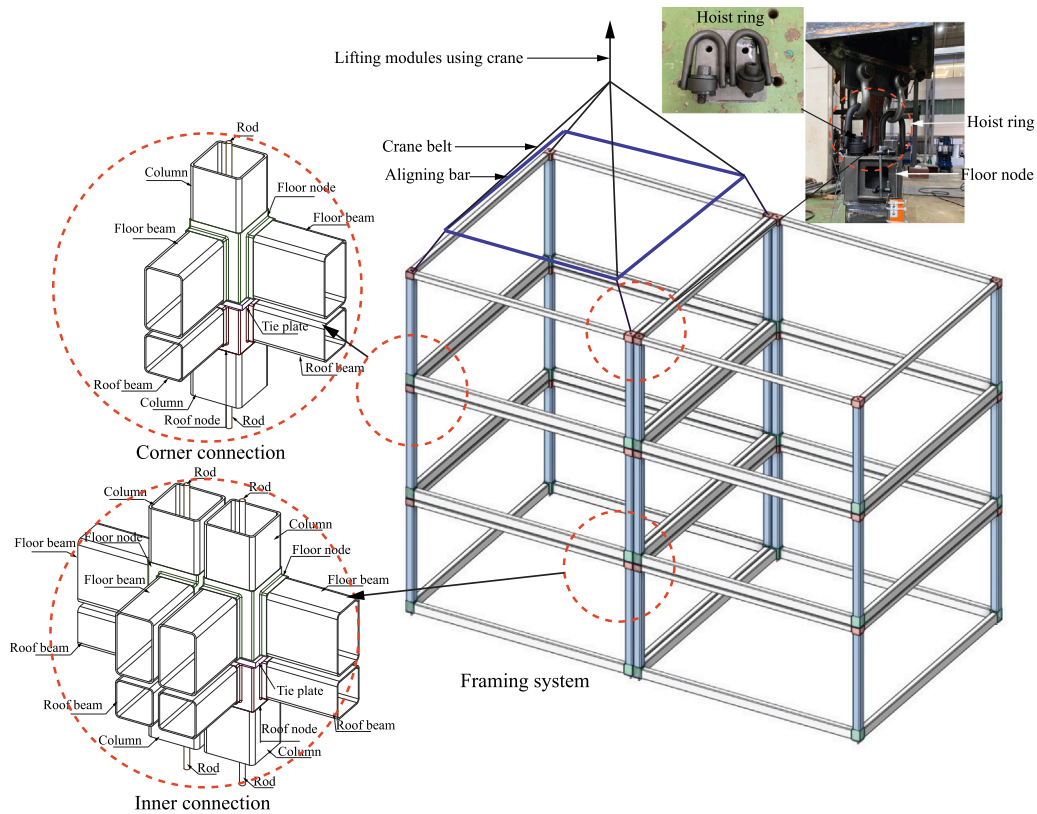


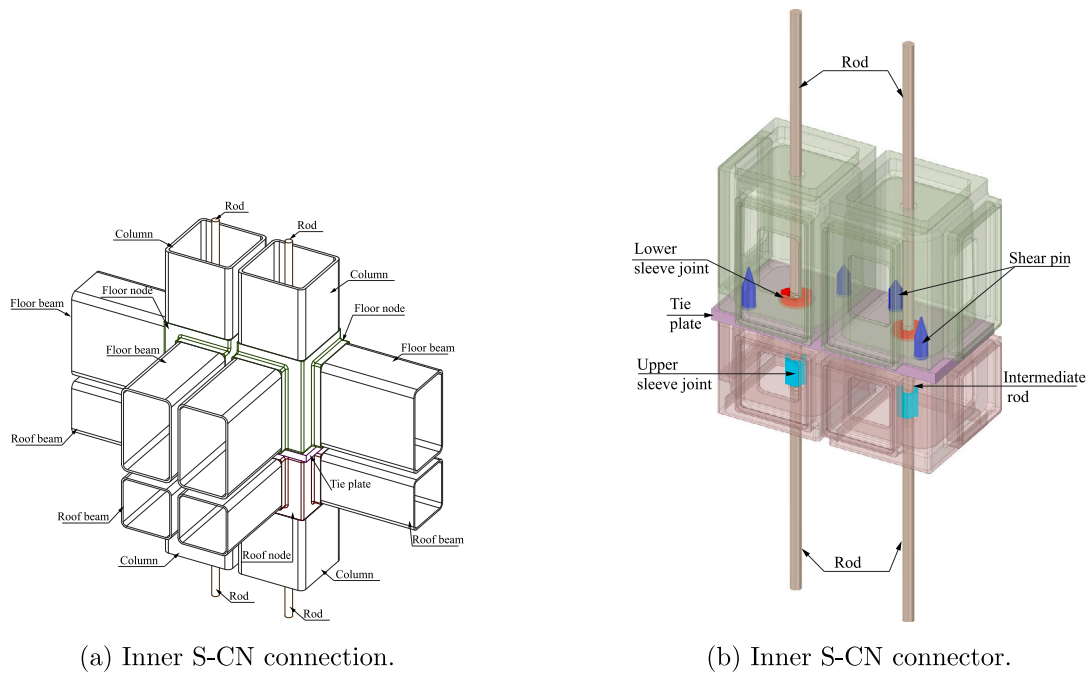
Fig. 2. Details of S-CN modular construction.

Han et al. has introduced a new methodology for constructing modular buildings with RHS members. Central to this innovation is the introduction of the S-CN connector, a cast-steel component that integrates tie rod and connector connection techniques. The unique attribute of the S-CN connector is its dual — purpose design, accommodating both beam-column and inter-modular connections, thus facilitating expedited on-site assembly. This connector consists of two primary components: floor and roof nodes produced using 3D printed sand molds and RHS members attached via welding (see Fig. 2 for details of S-CN modular construction). For transportation and on-site installation, these modules are designed with specialized holes to install hoist rings, facilitating efficient lifting at the four corners. This method is particularly advantageous for large-scale manufacturing: it streamlines transportation, minimizes lifting durations, and ensures straightforward horizontal and vertical assembly. Crucially, the comprehensive fabrication process for these modules transpires within

the factory environment, thereby eliminating supplementary on-site welding.

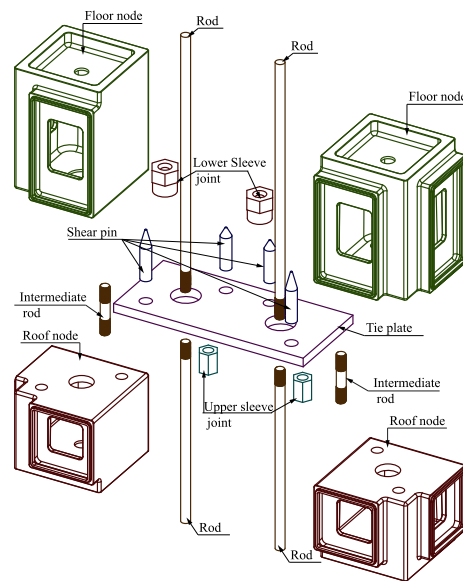
2.2. S-CN connector

The RHS modular framing system was developed in this study. The modules are stacked horizontally and vertically, with S-CN connectors connecting the modules at the corners, as shown in Fig. 3(a), Figs. 3(b), and 3(c) depict the S-CN connectors or node connectors of inner connections and their components. The floor and roof nodes are the connector’s fundamental components. The roof modular node connects the roof beams to the column, while the floor modular node connects the column to the floor beams. Each column, ceiling, and floor beams are made with RHS sections. All-around, full-penetration fillet welds



(a) Inner S-CN connection.

(b) Inner S-CN connector.



(c) Exploded image of the inner S-CN connector.

Fig. 3. Details of the inner S-CN connection.

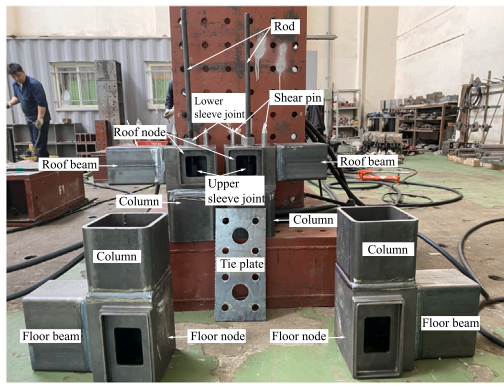
are utilized to join the modular nodes to the RHS sections. Two single-ended thread shear pins and a single-ended thread lower sleeve are fastened to the roof nodes when the modules are installed on-site.

An actual image of the S-CN connection is shown in Fig. 4(a). Two shear pins and the lower sleeve, shown in Fig. 4(b), are utilized to secure a tie plate to a roof node. The placement of the frame connection, such as the corner, edge, or interior, determines the size of the tie plate and the number of shear pins. The tie plate extends over and attaches to the floor node of horizontally adjacent modules, creating a horizontal connection between the modules. Subsequently, shear pins are connected to the floor node. These shear pins assist in aligning the top module over the bottom module during the vertical stacking of modules. With proper alignment of the top and bottom modules, the floor node and roof node are joined via a rod located inside the RHS

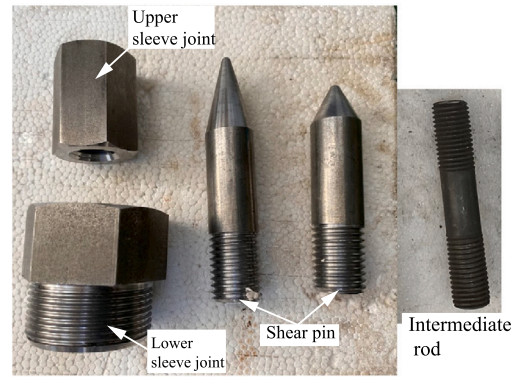
column. The threaded end of a rod is inserted into the threaded hole in the lower sleeve joint. Consequently, the vertical connection between the modules is established and secured appropriately.

Both VectorBloc and S-CN connections utilize molded and specifically shaped blocs or nodes to weld connections to RHS beams and columns. While they share these similarities, distinct differences exist. The advantages of the S-CN connection module structure are:

- **Simplicity:** The S-CN connector nodes have a more straightforward design in comparison to VectorBloc.
- **Vertical alignment:** The use of shear pins and rods in the S-CN system for vertical connections ensures that there is an accurate and uninterrupted vertical alignment throughout the assembled modules.



(a) S-CN connection.



(b) Sleeve joints, shear pins and intermediate rod.

Fig. 4. The actual image of a typical S-CN connection.

- **Architecture:** The components of the S-CN connector are positioned inside the RHS nodes and columns. This feature preserves the overall architectural appearance of the building as the connection components do not protrude externally.
- **Mechanical properties:** The S-CN connector's standout characteristic is the unequivocal force transmission capabilities. Compression forces are resisted by the nodes, tie plates, and RHS columns. Conversely, tensile forces are resisted by the nodes and rods, while shear forces are resisted through the combined action of rods and shear pins.

3. Finite element model development and validation

The experimental campaign of the S-CN connector performed by Han et al. is briefly summarized hereafter. Subsequently, the advanced FE model in ANSYS of the S-CN is described and validated against the experimental results. The FE model allows evaluating the significant parameters affecting the compressive behavior of the S-CN connector and connection.

3.1. Review of the experimental campaign

The research involved conducting experimental investigations on full-scale specimens of the S-CN connector and connection. The campaign focused on compressive tests. The key characteristics of the tests and the main results are briefly summarized herein to investigate the validation process.

3.1.1. Description of the test specimens and setup

Fig. 5 shows a detail of the specimens considered within the experimental campaign. The full-scale S-CN roof, floor node, S-CN connector, S-CN beam-column connection specimens were built and tested. A schematic of the S-CN roof and floor nodes with their outer dimensions is presented in Fig. 6.

The four specimens were subjected to axial compression load. The axial compression load was imposed using a vertical hydraulic actuator of 10,000-kN with a maximum stroke length of 250 mm, controlled by a load cell. In order to generate movement just in the vertical direction, this hydraulic actuator was fixed to a stiff steel reaction frame. The loading rate was approximately 0.5 kN until the maximum load was reached. Prior to reaching the maximum load, the loading rate was roughly 0.5 kN/s. When the stiffness lowered near the maximum load, the loading rate was decreased as far as possible to obtain the postpeak behavior.

The prototype connection was based on the typical parts of the actual building. 22 mm diameter steel rods and 24 mm shear pins were adopted. Key information about the geometric properties of the RHS section is given in Table 1.

Table 1
Geometric properties of the RHS sections.

RHS section	Width (mm)	Depth (mm)	Thickness (mm)
RHS floor beam	150	250	5
RHS roof beam	150	150	5
RHS column	200	200	10

3.1.2. Material properties

The specimens were of the same steel grade components as the prototype structure. The unit floor and roof nodes and RHS column were made of SCW550 steel in accordance with the Korean standards, while the RHS beam members were made of S275 steel. Other components were made of S45C steel. Key information about the mechanical properties of the specimen components is given in Table 2.

The engineering stress-strain relationship obtained from the tensile tests of the steels in this study is described using the bilinear plus nonlinear hardening model proposed by Yun and Gardner [40]. The choice of this model is influenced by the absence of additional tensile tests, highlighting the need for a suitable approach to accurately characterize the steel's behavior.

The bilinear plus nonlinear hardening model [40]:

$$\sigma(\epsilon) = \begin{cases} E\epsilon & \text{for } \epsilon \leq \epsilon_y \\ F_y & \text{for } \epsilon_y < \epsilon \leq \epsilon_{sh} \\ F_y + (F_u - F_y) \left\{ 0.4 \left(\frac{\epsilon - \epsilon_{sh}}{\epsilon_u - \epsilon_{sh}} + \right) + 2 \left(\frac{\epsilon - \epsilon_{sh}}{\epsilon_u - \epsilon_{sh}} \right) / [1 + 400 \left(\frac{\epsilon - \epsilon_{sh}}{\epsilon_u - \epsilon_{sh}} \right)^5]^{1/5} \right\} & \text{for } \epsilon_{sh} < \epsilon \leq \epsilon_u \end{cases} \quad (1)$$

$$\epsilon_u = 0.6 \left(1 - \frac{F_y}{F_u} \right) \quad (2)$$

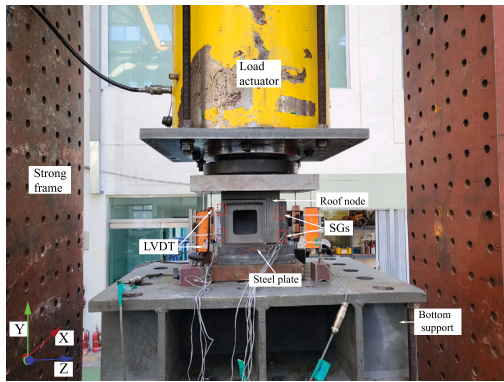
But $\epsilon_u \geq 0.06$ for hot-rolled steels

$$\epsilon_{sh} = 0.1 \frac{F_y}{F_u} - 0.055 \quad (3)$$

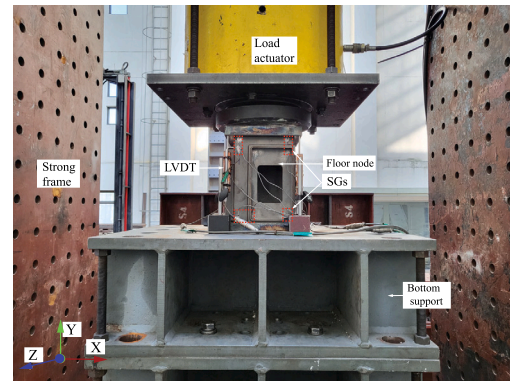
But $0.015 \leq \epsilon_{sh} \leq 0.03$ where: E - Young's modulus; F_y - yield stress and the corresponding yield strain ϵ_y ; ϵ_{sh} - strain hardening strain; F_u - the ultimate tensile stress and the corresponding ultimate tensile strain ϵ_u [41].

The stress and strain obtained by the tensile test are transformed into the true stress and strain using the following equation [42]:

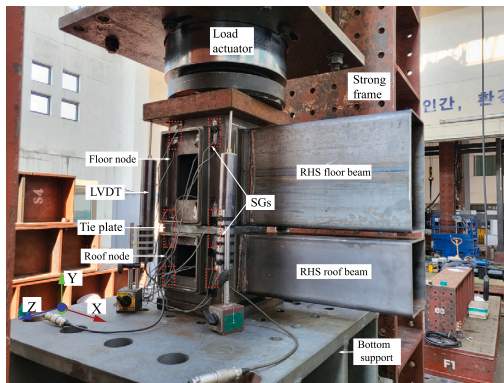
$$\sigma_{true} = \sigma(1 + \epsilon) \quad (4)$$



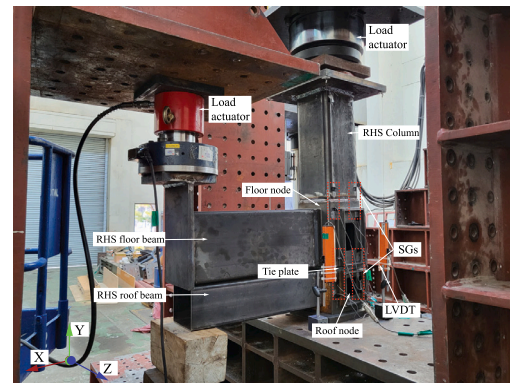
(a) Roof node.



(b) Floor node.

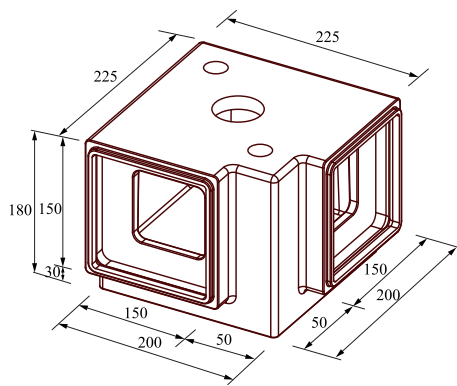


(c) S-CN connector.

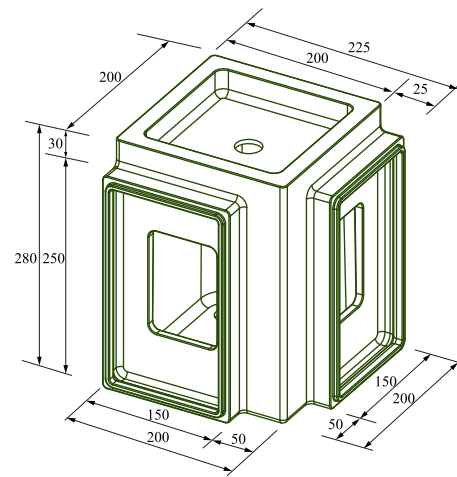


(d) S-CN beam-column connection.

Fig. 5. Experimental test of the S-CN connection.



(a) Roof modular nodes.



(b) Floor modular nodes.

Fig. 6. Dimensions of floor modular nodes and roof modular nodes.

Table 2
Mechanical properties of the specimen components.

Component	Material specification	Young's modulus (E) (GPa)	Yield strength (F_y) (MPa)	Ultimate strength (F_u) (MPa)
Floor and roof nodes	SCW550	205	509	649
RHS floor and roof beams	S275	203	275	430
RHS column	SCW550	205	509	649
Tie plate	S45C	205	490	686
Lower and upper sleeve joint	S45C	205	490	686
Rod and intermediate rod	S45C	205	490	686
Shear pin	S45C	205	490	686

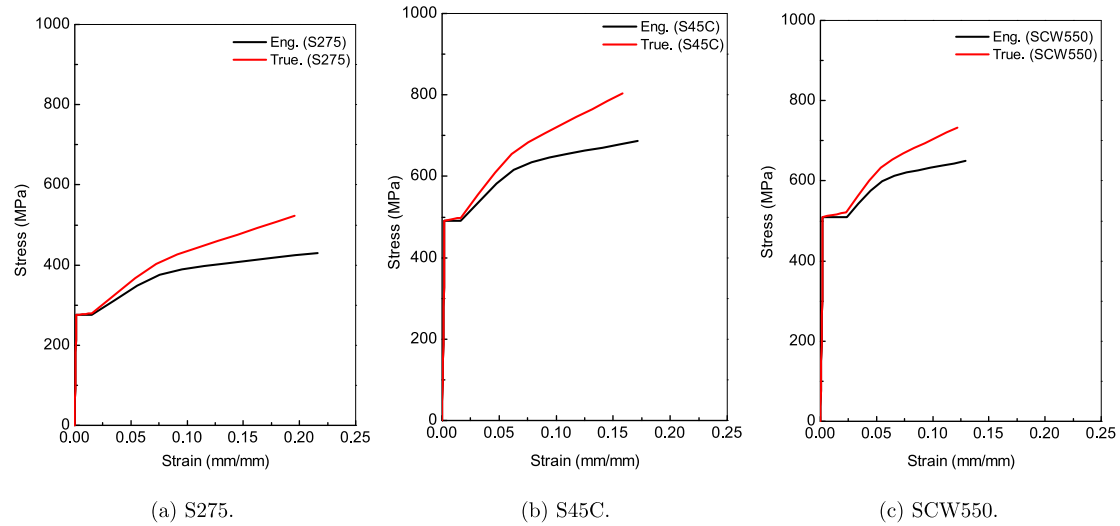


Fig. 7. Engineering and true stress–strain curves.

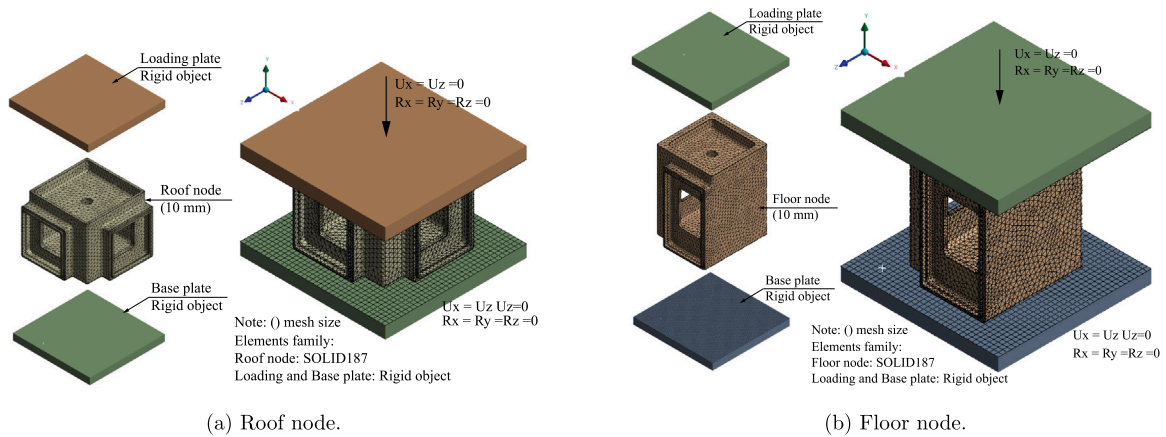


Fig. 8. The FE models of the two modular node specimens.

$$\epsilon_{true} = \ln(1 + \epsilon) \tag{5}$$

Fig. 7 illustrates the stress–strain relationships obtained from the engineering and true stress–strain curves that were used in the FE simulations.

3.2. Modeling assumption

This study established FE models based on software tool ANSYS Mechanical Enterprise 2021/R1 [43]. Fig. 8 shows the ANSYS modeling image of the modular roof and floor specimens [36].

Fig. 9 describes the modeling approach used to study the structural behavior of a connector specimen under axial compression load.

Fig. 10 describes the FE model used to study the structural behavior of a beam–column specimen under axial compression load.

The FE model dimensions were derived from the test specimen. All model nonlinearities – material, geometric, and contact – were incorporated. The Von Mises yield criterion, integrated with the Multilinear Isotropic Hardening material model [44] and isotropic strain hardening, was employed. Stress–strain relationship defining points were informed by Table 2 and Fig. 7. The input generation MATLAB code for the ANSYS Multi-Linear Isotropic Hardening Model is detailed in Appendix.

Components were modeled using ANSYS's 3D 20-node solid elements (SOLID186) and 3D 10-node elements (SOLID187) [36]. Both loading and base plates were treated as rigid, negating deformations during simulations for analytical simplicity. Contact interfaces between

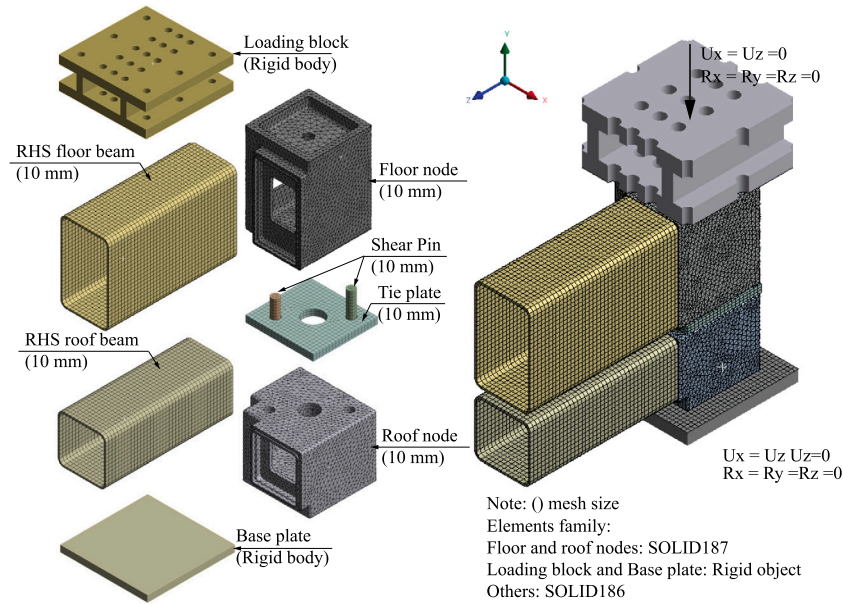


Fig. 9. FE model of the S-CN connector specimen.

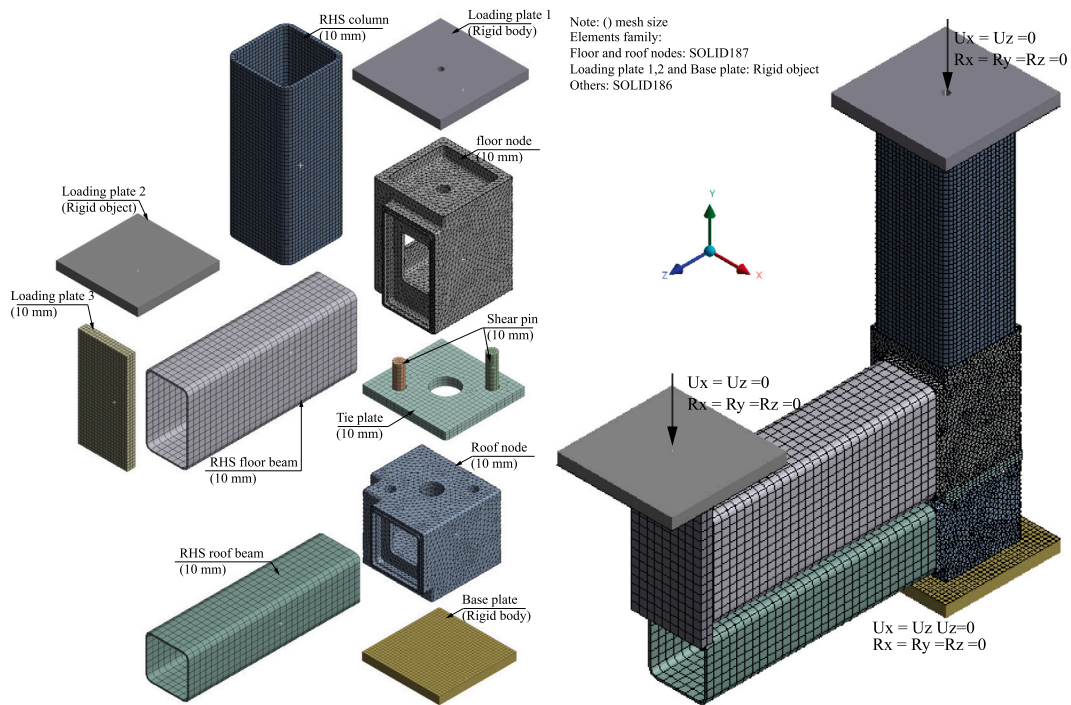


Fig. 10. FE model of the beam-column connection specimen.

the specimen-loading plate and specimen-base plate were defined using CONTA174 and TARGE170 elements. A friction coefficient of 0.30 was set for steel part interfaces (including base plate, shear pin, roof node, floor node, and column), aligned with EN 1090-2 standards [45]. Bonded contact was employed for surfaces between modular nodes, RHS beams, shear pins, and the roof node. The base plate bottom was fixed to ensure specimen stability.

A mesh sensitivity analysis was performed to determine the optimal mesh size, balancing result accuracy and computational efficiency. Four element sizes, from 5 mm to 20 mm, were evaluated for modeling the floor and roof nodes. Fig. 11 presents the load-displacement curves for various mesh sizes. The curves demonstrate that the variation in mesh size exerts limited influence on the elastic stage of the load-displacement curve obtained by FEA. The data indicates that while

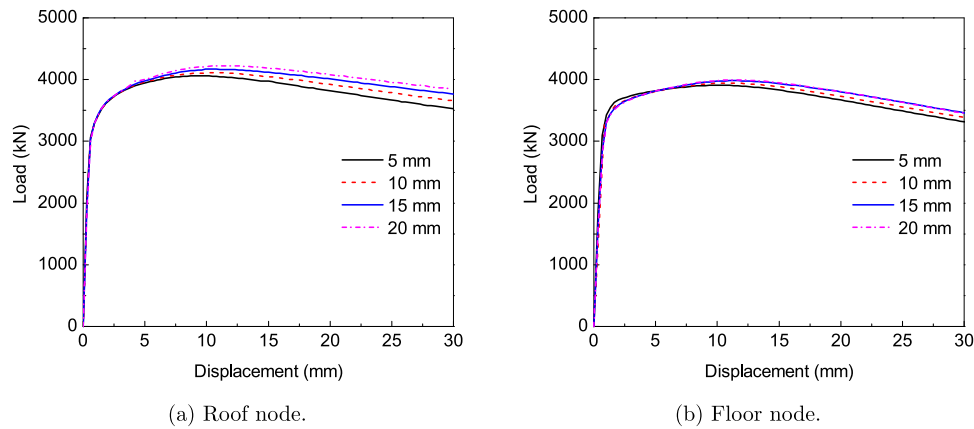


Fig. 11. Mesh sensitivity analysis of load–displacement results for different element sizes.

peak loads remained relatively consistent across different mesh sizes, post-peak behaviors exhibited variation. For the roof node, the ultimate loads corresponding to these sizes were 4059.6 kN, 4111.4 kN, 4160.4 kN, and 4204.50 kN, respectively, signifying a 3.6% load variation upon increasing the element size from 5 mm to 20 mm. In contrast, for the floor node, the respective loads were 3909.3 kN, 3942.5 kN, 3981.80 kN, and 3995.30 kN, resulting in a 2.2% variation across the same size range. Given these findings, a 10 mm element size was selected for all components across the four specimens to ensure a balance of precision and computational efficiency.

A displacement-controlled approach was adopted, with test displacements extending up to 50 mm. Non-linear equilibrium equations were addressed via the Static Structural module. The Full Newton–Raphson method was chosen for solution, incorporating an auto-incrementation for load application. The initial increment size was set to 1 mm, with minimum and maximum values of 0.05 mm and 1 mm, respectively. Large deflection considerations were activated during analysis.

Geometrical imperfections of floor and roof nodes were considered in the model, focusing on local imperfections. These were defined by scaling the local buckling eigenmode [46] using Eigenvalue Buckling module in ANSYS. Due to limited information, manufacturing tolerances [47] or the value of $d/150$ (where d is the height of the node wall) from Kim and Lee [48] were used as a substitute for simulating actual imperfections.

3.3. Validation

3.3.1. Modular node specimens

Figs. 12 and 13 depict the failure mode test results and analysis results of modular roof node and modular floor node specimens. The analysis compared the load-deformation relationships from the tests and analyses. The results of the von Mises stresses and deformation modes at peak Point A and postpeak Point B are shown in Figs. 12(c,d) and 13(c,d). The agreements between the analyses and tests varied from specimen to specimen.

- For the modular roof node specimen (see Fig. 12), the FE analysis closely aligned with experimental results. The FE model accurately predicted the yield and ultimate loads under compression as 3758 kN and 4111.40 kN, respectively. These predictions were in close agreement with the experimental values of 3594 kN and 4445.22 kN, respectively. The errors in the predicted yield and ultimate loads were 4.56% (see Table 3) and 7.51% (see Table 4), respectively. The predicted failure mode, characterized by local buckling around the opening and crippling of the casting roof node sidewalls, also matched test observations.

Table 3

Comparison of experimental load-bearing capacities (yield loads) with AISC 360-16 and FEA predictions.

No.	Specimen	Yield load (kN)			Error (%)	
		Test	AISC 360-16	FEA	AISC-360-16	FEA
1	Roof node	3594.00	3313.32	3758.00	7.81	4.56
2	Floor node	3477.00	3265.76	3721.00	6.08	7.02
3	S-CN connector	3290.00	3265.76	3325.00	0.74	1.06
4	Beam-column	3495.00	3265.76	3224.00	6.56	7.75

Table 4

Comparison of experimental load-bearing capacities (ultimate loads) with FEA predictions.

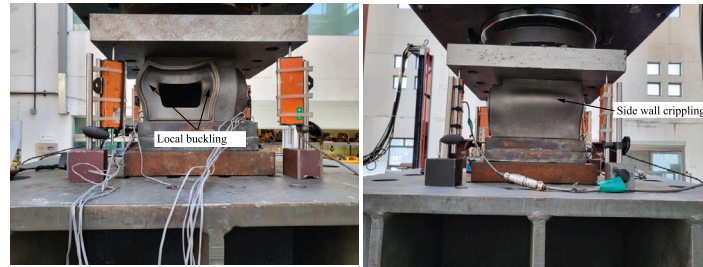
No.	Specimen	Ultimate load (kN)		Error (%)
		Test	FEA	FEA
1	Roof node	4445.22	4111.40	7.51
2	Floor node	4029.06	3942.50	2.15
3	S-CN connector	3575.00	3883.90	8.64
4	Beam-column	3974.00	3916.00	1.46

- For the modular floor node specimen (refer to Fig. 13), the FE analysis yielded load–displacement predictions consistent with experimental observations. The FE model predicted the yield load and ultimate load under compression as 3721 kN and 3942.50 kN, respectively. These values align closely with experimental measurements of 3477 kN and 4029.09 kN for the yield and ultimate loads, respectively. The deviations from the experimental results were 7.02% for the yield load (refer to Table 3) and 2.15% for the ultimate load (refer to Table 4). However, discrepancies emerged in predicted failure modes. While the FE model expected failure due to local buckling and wall crippling at the casting floor node, experiments showed rupture at the openings. Such disparities may arise from the inherent limitations of ANSYS static analysis or potential craftsmanship-induced weaknesses.

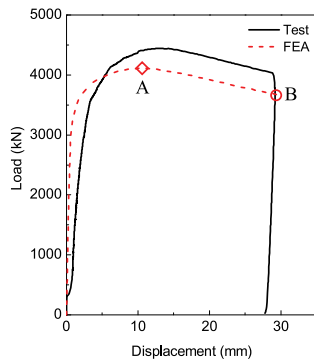
3.3.2. S-CN connector specimen

Fig. 14 shows the analysis results of the connector specimen. Fig. 14(b) shows the load-deformation relationships for the tests and analyses.

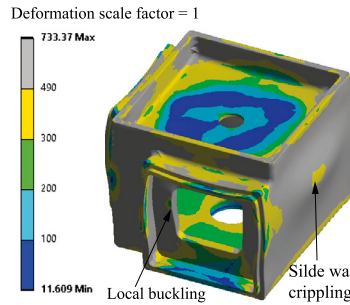
The FE analysis aligned well with experimental outcomes. The FE model predicted yield and ultimate compressive loads of 3325 kN and 3883.90 kN, respectively, closely correlating with observed values of 3290 kN and 3757 kN. The errors from the experimental results were 1.06% for the yield load (refer to Table 3) and 8.64% for the ultimate load (refer to Table 4). Results for von Mises stresses and deformation modes at peak Point A and postpeak Point B can be



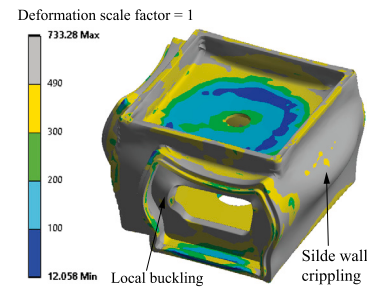
(a) Failure mode.



(b) Load-deformation behavior

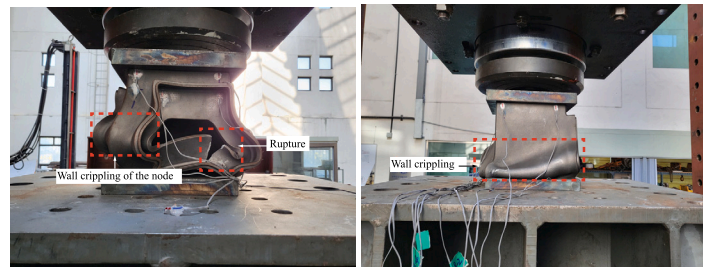


(c) Peak Point A.

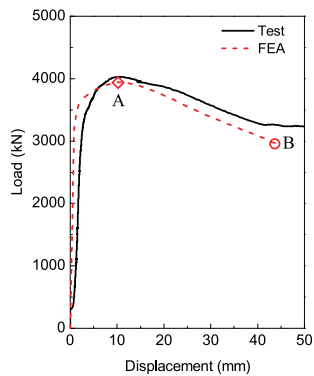


(d) Postpeak Point B.

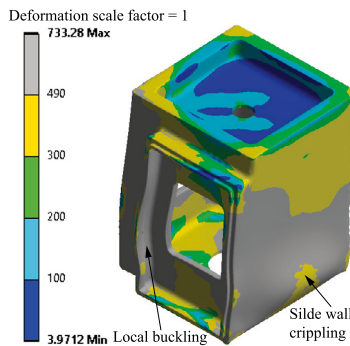
Fig. 12. Test and analysis results of modular roof specimen: (a) Failure mode, (b) load-deformation relations; and analysis results of von Mises stresses and deformation modes (c,d).



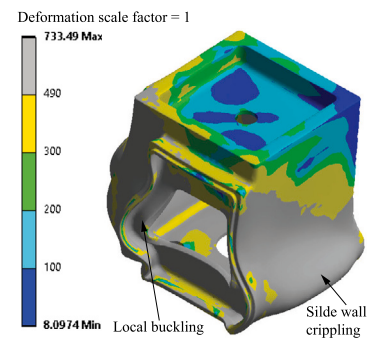
(a) Failure mode.



(b) Load-deformation behavior



(c) Peak Point A.



(d) Postpeak Point B.

Fig. 13. Test and analysis results of modular floor specimen: (a) Failure mode, (b) load-deformation relations; and analysis results of von Mises stresses and deformation modes (c,d).

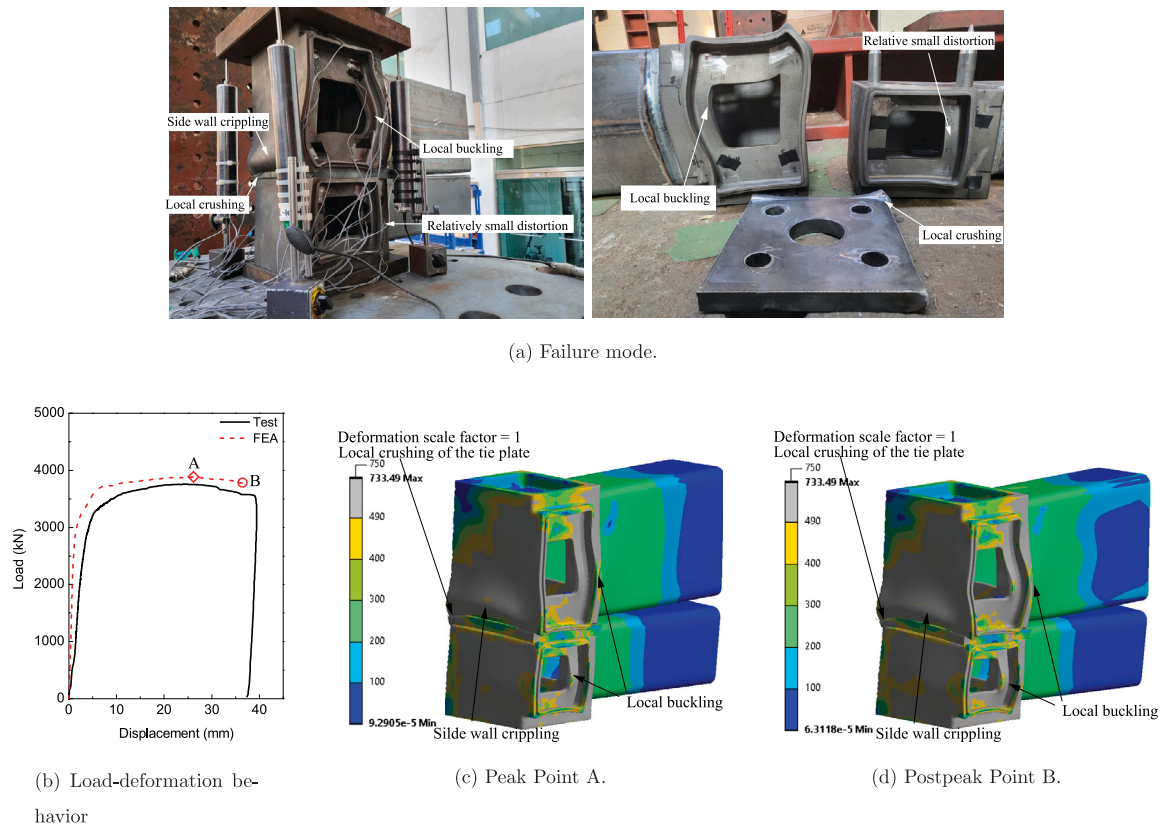


Fig. 14. Test and analysis results of the S-CN connector specimen: (a) load-deformation relations; and analysis results of von Mises stresses and deformation modes (c,d).

found in Fig. 14(c,d). Observed failure modes, such as local buckling around openings and crippling of casting floor node sidewalls, matched FE predictions. Furthermore, the model accurately described the local crushing failure mode of the tie plate. Overall, the FE model effectively replicated specimen behavior under compressive loading.

3.3.3. Beam-column connection specimen

Fig. 15 shows the analysis results for a connector specimen. Fig. 15(b) shows the load-deformation relationships between the tests and analyses.

The FE analysis yielded predictions of yield and ultimate compressive loads as 3224 kN and 3916 kN, respectively, which were in proximity to the experimental results of 3495 kN and 3974 kN. The errors from the experimental results were 7.75% for the yield load (refer to Table 3) and 1.46% for the ultimate load (refer to Table 4). Refer to Fig. 15(c,d) for the von Mises stresses and deformation modes at both peak Point A and postpeak Point B. The anticipated failure modes, including local buckling around openings and crippling of casting floor node sidewalls, were consistent with test findings. The model's depiction of the tie plate's local crushing failure mode also matched experimental observations. Nonetheless, the FE model's prediction for displacement at Peak Point Load showed some deviation. Overall, the FE models effectively captured the compressive loading behavior of the specimens.

4. Load-bearing capacity evaluation of the S-CN connector using AISC 360-16

This section discusses the evaluation of the compressive load-bearing capacity of the S-CN connections in accordance with the current design code provisions in AISC 360-16 [49]. In order to calculate the load-bearing capacity, S-CN node hollow section at the opening position and column cross section are idealized and simplified, as

shown in Fig. 16. This simplification was made for ease in calculating the load capacities.

According to Table E1.1 AISC 360-16, the nominal compressive strength, P_{nc} , of the sections in this study shall be the lowest value derived based on the applicable limit states of flexural buckling and flexural-torsional buckling for the node sections and the flexural buckling for RHS column section.

The nominal compressive strength, P_{nc} , based on the limit state of flexural buckling shall be determined based on the limit states of torsional and flexural-torsional buckling, can be calculated using Eq. (6) [49,50].

$$P_{nc} = F_{cr} A_g \tag{6}$$

where A_g — gross section area of the node section, F_{cr} — flexural or flexural-torsional buckling stress.

- For the nominal compressive strength based on the limit state of flexural buckling:

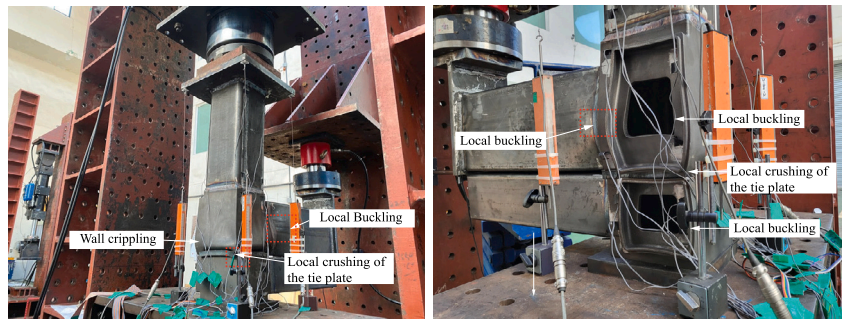
$$F_{cr} = \min\{0.658 \frac{F_y}{F_e} F_y, 0.877 F_e\} \tag{7}$$

$$F_e = \frac{\pi^2 E}{(\frac{KL}{r})^2} \tag{8}$$

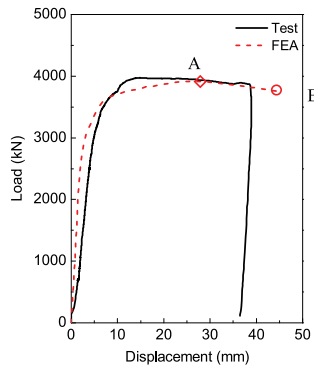
where K — effective length factor for flexural buckling; L — length of the walls of the node; r — radius of gyration of the node section about the weak axis; and F_e — elastic buckling stress determined according to Eq. (8).

- For the nominal compressive strength based on the limit state of flexural-torsional buckling: The critical stress, F_{cr} , shall be determined according to Eq. (7). The torsional or flexural-torsional elastic buckling stress, F_e , determined using equation E4-2 of AISC 360-16 as follows:

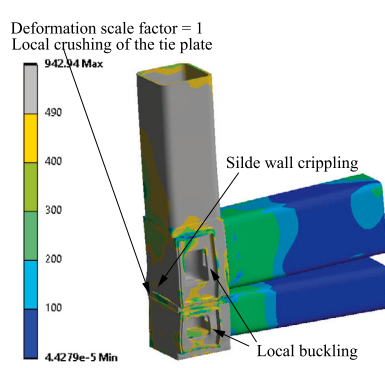
$$F_e = \left(\frac{\pi^2 EC_w}{L_{cy}^2} + GJ \right) \frac{1}{I_x + I_z} \tag{9}$$



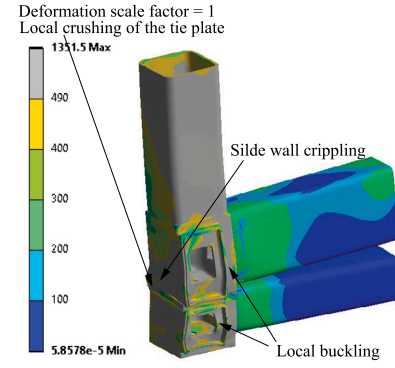
(a) Failure mode.



(b) Load-deformation behavior

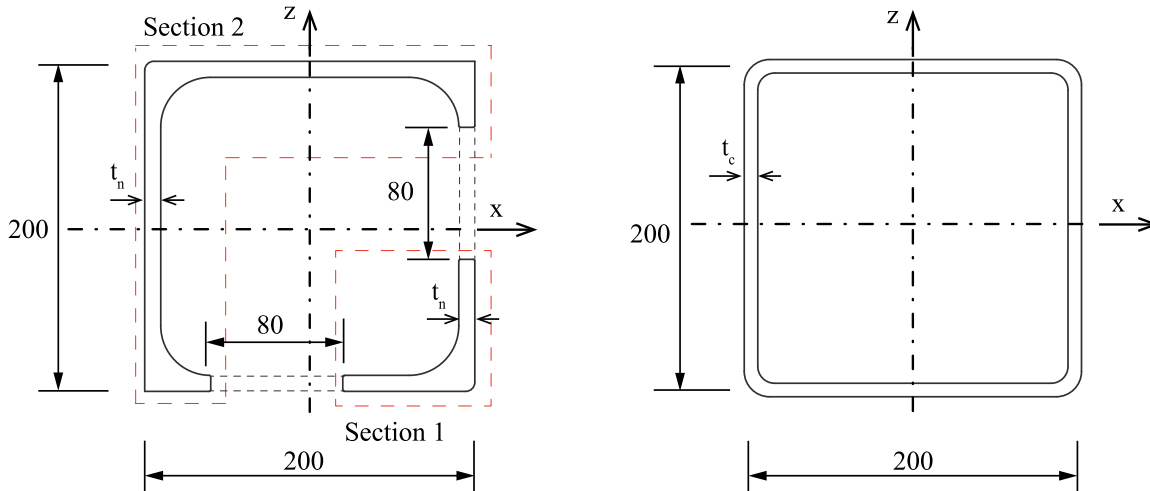


(c) Peak Point A.



(d) Postpeak Point B.

Fig. 15. Test and analysis results of the beam–column connection specimen: (a) load-deformation relations; and analysis results of von Mises stresses and deformation modes (c,d).



(a) The nodes at the opening

(b) RHS column.

Fig. 16. Simplified section geometry of the nodes and the RHS column.

where C_w - warping constant; G - shear modulus of elasticity of steel; I_x, I_z - moment of inertia about the principal axes; $L_{ey} = K_y L_y$ effective length of member for buckling about longitudinal axis; and J - torsional constant.

As shown in Fig. 16(a), the nominal strength of the floor node, roof node was calculated by adding the nominal strengths of the sections 1 and 2. The nominal compressive strength, P_{nc} , shall be determined based on the limit states of torsional and flexural–torsional buckling using Eq. (6).

Similarly, in Fig. 16(b), the nominal compressive strength of RHS column, P_{nc} , shall be determined based on the limit states of torsional and flexural–torsional buckling using Eq. (6).

The compressive load-bearing capacity of the S-CN connector is determined by selecting the lower value between the design load-bearing capacities of the roof and floor nodes. The design load-bearing capacity of the beam–column connection is determined by selecting the minimum value among the load-bearing capacities of the roof node, floor node, and RHS column. Fig. 17 depicts the proposed process of

Table 5
Load-bearing evaluation of the specimens using AISC 360-16.

Components	Section	b/t or D/t	λ_r	Limit states		Predicted load-bearing capacity (kN)
				FB (kN)	FTB (kN)	
Roof node	1	20.75	14.25	2500.97	2490.26	3313.32
	2	8.30	14.25	823.06	-	
Floor node	1	22.22	14.25	2365.75	2328.26	3265.76
	2	8.89	14.25	937.50	-	
RHS column	RHS	3.00	44.00	3665.22	-	3665.22
Connector	-	-	-	-	-	3265.76
Beam-column connection	-	-	-	-	-	3265.76

FB: Flexural buckling ; FTB: Flexural-torsional buckling;
b/t or D/t: The width-to-thickness; λ_r : The limiting width-to-thickness.

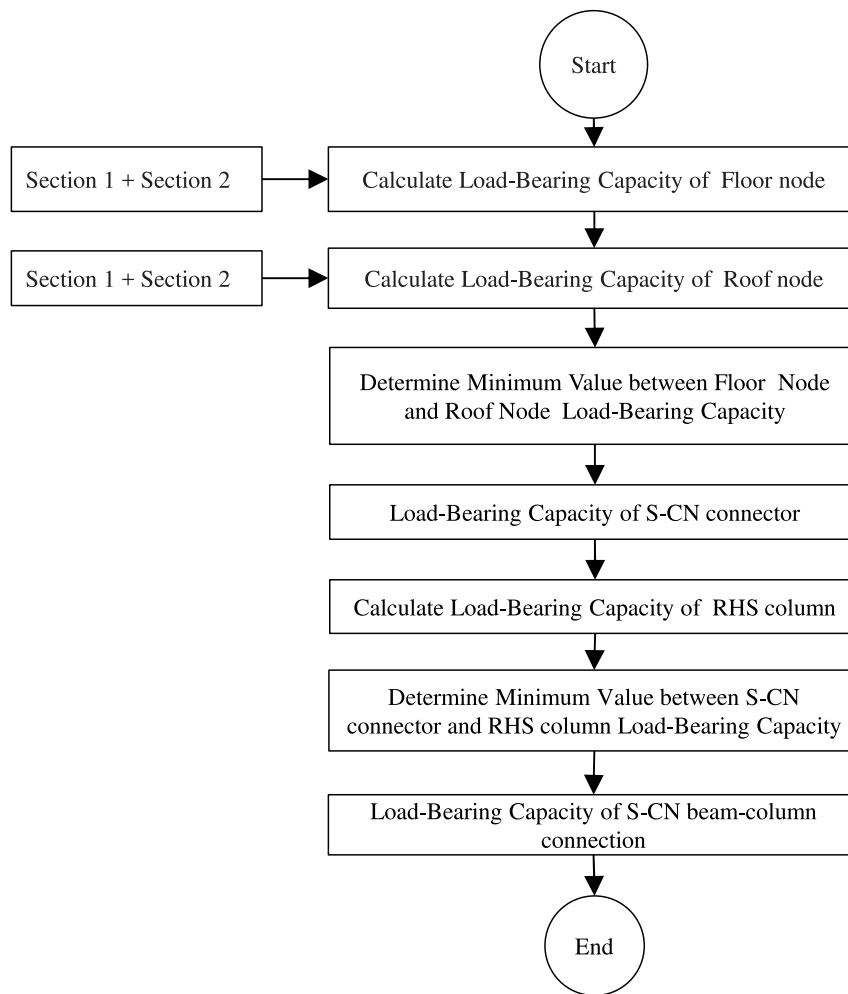


Fig. 17. The process of determining the compressive load-bearing capacity of the S-CN connection based on AISC 360-16.

determining the compressive load-bearing capacity of the connection nodes, the S-CN connector, and the beam-column connection.

The process for determining the load capacity of the specimens in accordance with AISC 360-16 in this study is outlined in Table 5. Fig. 18 and Table 3 compare the predicted load-bearing capacities of the specimens with test results. The comparison results can be summarized as follows:

- As per the AISC 360-16 calculations for compressive load-bearing capacity of floor and roof node specimens, it has been determined

that the primary reason for failure is the torsional or flexural-torsional elastic buckling method at the openings. This finding is in line with the results obtained from the corresponding experiments. Additionally, the computation also indicates that the failure of S-CN connector and beam-column connection specimens is anticipated to occur at floor nodes similar to the findings from experiments.

- Using a simplified computational model based on the AISC 360-16 standard, the load-bearing capacities of the floor node, roof node, S-CN connector, and S-CN beam-column connection specimens were found to be consistent with the predictions set forth

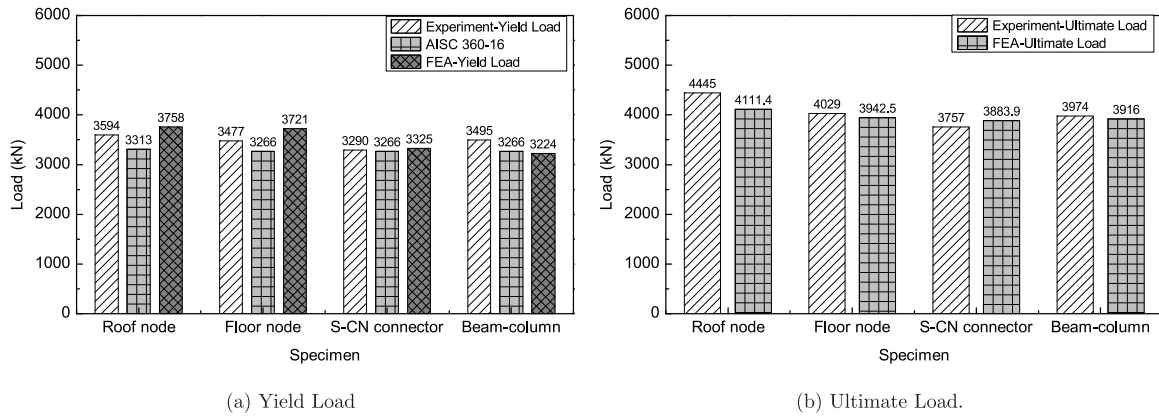


Fig. 18. Comparison between the load-bearing capacity values obtained from experimental tests with those predicted by AISC 360-16 and FEA.

Table 6
Values of the parameters.

No	Specimen	Parameter	Values	Notation
1	Connector	Thickness of the wall of the node (TN)	9 mm, 8 mm, 7 mm, 6 mm, 5 mm, 4 mm	9TN, 8TN, 7TN, 6TN, 5TN, 4TN
		Thickness of a tie plate	24 mm, 20 mm, 16 mm, 12 mm, 8 mm, 4 mm	24TP, 20TP, 16TP 12TP, 8TP, 4TP
2	Beam-column	Thickness of the wall of the node (TN)	9 mm, 8 mm, 7 mm, 6 mm, 5 mm, 4 mm	9TN, 8TN, 7TN, 6TN, 5TN, 4TN
		Thickness of a column	12 mm, 11 mm, 10 mm, 9 mm, 8 mm, 7 mm	12C, 11C, 10C, 9C, 8C, 7C

by the AISC 360-16 standard. Specifically, the AISC 360-16 predicted capacities for the roof node, floor node, connector, and beam-column specimens were 3313.32 kN, 3265.76 kN, 3265.76 kN, and 3265.76 kN, respectively. These estimates align closely with the experimental outcomes, which were 3594 kN, 3477 kN, 3290 kN, and 3495 kN. The observed discrepancies between the predicted and experimental data were 7.81%, 6.08%, 0.74%, and 6.56% for each specimen, in that order.

- These findings not only validate the reliability of both computational and empirical approaches but also underscore the distinct unambiguous transmission capabilities of the S-CN connection. Furthermore, the results support the application of the AISC standard in the design process of the S-CN connector when subjected to compressive loads.

5. Parametric study

This section discusses the factors that affect the performance of the connector when subjected to axial compression loading. Table 6 presents the values of the parameters chosen in the parametric study. This table shows that 24 different FE models were considered in the parametric study of the connector and beam-column specimens, each with a different combination of tie plate and the column thicknesses, and the thickness of the wall of the connection nodes. The models are identified with notations presented in this table.

In the study, six different thicknesses were examined for the tie plate, connection nodes, and column. For instance, the connector specimen model with a tie plate thickness of 24 mm and the two original modular nodes tested in this study were denoted as “24TP”. Similarly, the beam-column specimen model with a column thickness of 9 mm and the original tested connector were represented as “9C”.

5.1. S-CN connector specimen

A parametric study was conducted on a connector specimen. In this study, the ultimate load is defined as the FE model’s highest load

capacity, and the yield load is the load at which plastic deformation begins in the FE model. The load was applied to the FE model by applying axial displacement. The connector specimen deformed axially as the axial load increased, and upon reaching the maximum load, the two modular nodes buckled inelastically and the tie plate was crushed locally.

Fig. 19(a) demonstrates the relationship between changes in the tie plate’s thickness and the axial compressive behavior of the S-CN connector specimen. The figure indicates that as long as the thickness of the two modular nodes are unchanged, altering the tie plate’s thickness does not affect the axial compressive behavior of the connection.

On the other hand, Fig. 19(b) depicts the correlation between axial compressive load and axial displacement at the loading block of the FE model, with varying thicknesses of the two connection nodes. In all FE models subjected to axial compression loads, the plastic strains first occurred in the floor modular node. Also, reducing the thickness of the nodes unequivocally resulted in a decrease in the bearing capacity of the connector. This demonstrates a clear correlation between the node thickness and the connector’s load-carrying capability.

Fig. 20(a) illustrates the yield and ultimate loads of the FE model as the thickness of the connection nodes varies from 9 mm to 4 mm. Notably, as the thickness of the two modular nodes decreased by 0 to 5 mm, the ultimate load capacity of the connection decreased by 0% to 46%. The relationship between node thickness and yield and ultimate load capacities of the connector was nearly linear, with R-square values of 0.996 and 0.997, respectively.

Additionally, the relationship between node thickness and reductions in yield and ultimate load capacities of the connector is further presented in Fig. 20(b). The reduction in yield and ultimate load capacities was evaluated concerning the validated reference model. The findings from this parameter study serve as a foundation to determine the optimal thickness of the two modular nodes for optimizing the connection’s load-bearing capacity.

5.2. Beam-column connection specimen

This study presents a parametric investigation of a beam-column connection specimen subjected to an axial compressive load. As the

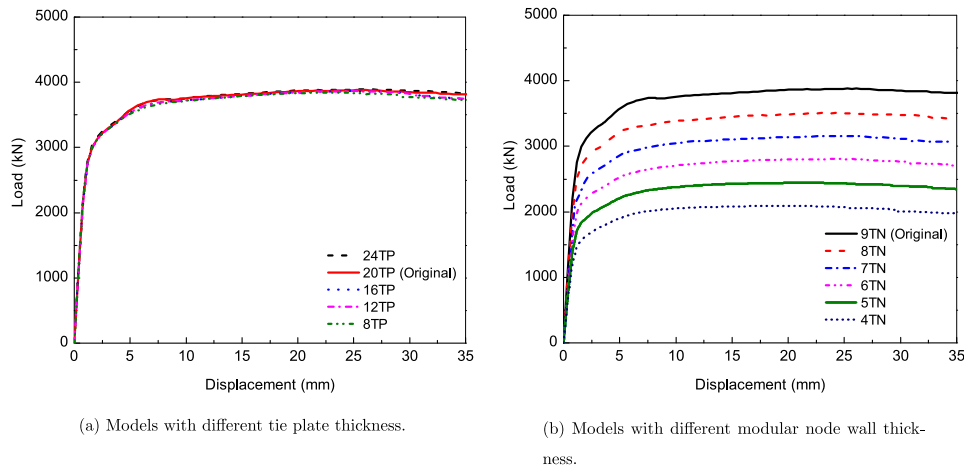


Fig. 19. Compression load–displacement behavior.

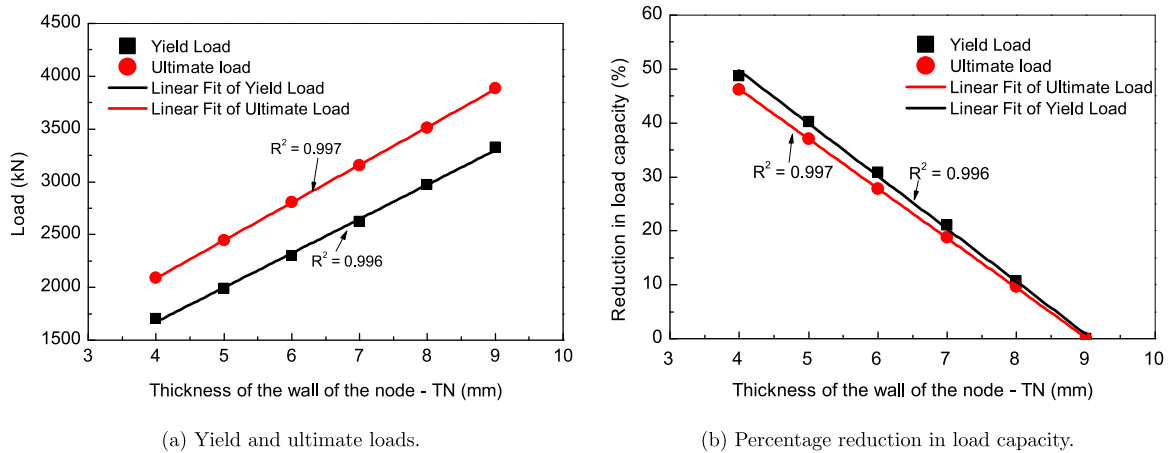


Fig. 20. Effect of thickness reduction of the tie plate and wall of the modular nodes on axial compression capacity.

axial load increased, the beam–column specimen deformed axially until reaching the maximum load.

The study investigated the correlation between the column’s thickness and the axial compressive behavior of the beam–column specimen, as shown in Fig. 21(a), while keeping the thickness of the two modular nodes and tie plate unchanged. The results indicate a clear dependence of the connection’s compressive capacity and failure mode on the column’s wall thickness.

- As the thickness of the column increased from 10 mm to 11 mm, and 12 mm, the ultimate compressive resistance of the specimen slightly increased by 0.67%, and 0.45% respectively. In these cases, after reaching the inelastic bearing capacity, displacement kept increasing and the strength decreased slowly.
- As the column thickness was decreased from 10 mm to 9 mm, 8 mm, and 7 mm, the ultimate compressive force of the specimen significantly decreased by 10.41%, 23.08%, and 33.34%, respectively. Therefore, in these cases, reducing the column thickness from 10 to 7 mm had a significant impact on the displacement of the models at peak load, leading to a significant reduction in the corresponding displacement at maximum load. After reaching the ultimate load, displacement kept increasing and the strength rapidly degraded due to local buckling.

- The failure mode of the specimens varied depending the RHS column from local buckling of the nodes and local crushing of the tie plate (Specimen 12C, 11C, and 10C) to a combination of local buckling of columns and modular nodes (Specimen 9C) and fully dominant local buckling of the columns in Specimens 8C and 7C, as shown in Fig. 22. As the thickness of the column decreased, early inelastic buckling occurred and the ultimate load capacity of the connection was reduced.
- Consequently, the parametric study suggests that to optimize the structure’s bearing capacity, the designer must choose suitable sizes for the columns, and connectors.

The study conducted an analysis of a FE model under axial compressive load, considering varying connection node thickness. Fig. 21(b) illustrates the relationship between axial compressive load and axial displacement at the loading block of the FE model. Notably, plastic strains were observed to first occur in the floor modular node for all FE models subjected to axial compression loads. Also, reducing the thickness of the nodes unequivocally resulted in a decrease in the bearing capacity of the connector.

The yield and ultimate loads obtained from the FE models were then evaluated in relation to the thickness of the node’s wall, as shown in Fig. 23(a). Notably, as the thickness of the two modular nodes

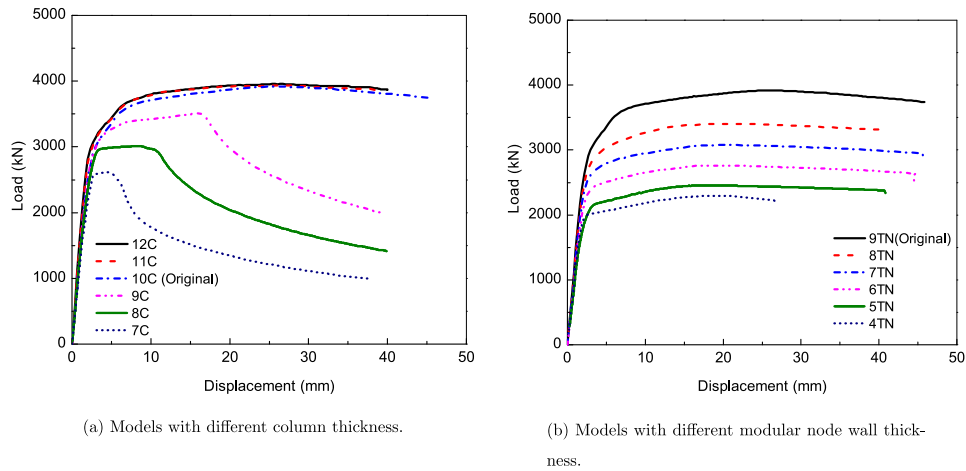


Fig. 21. Compression load–displacement behavior.

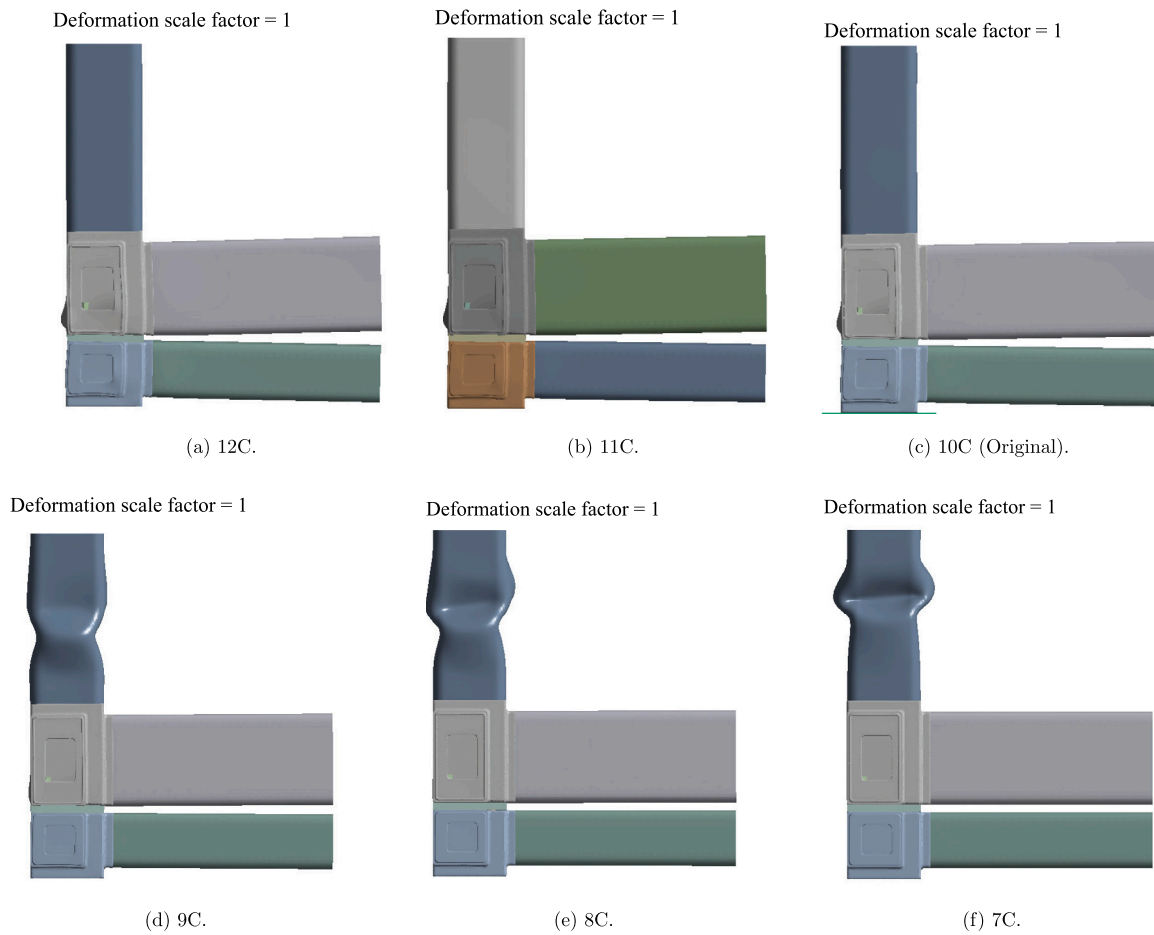


Fig. 22. The failure mode of the beam–column specimen with different column's thickness.

decreased by 0 to 5 mm, the ultimate load capacity of the beam–column connection decreased by 0% to 46%. The relationship between node

thickness and yield and ultimate load capacities of the connector was nearly linear, with R-square values of 0.991 and 0.973, respectively.

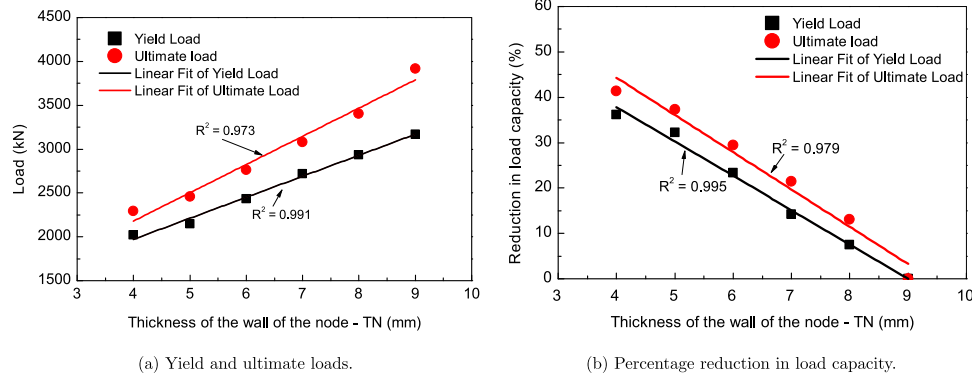


Fig. 23. Effect of thickness reduction of the tie plate and wall of the modular nodes on axial compression capacity.

Furthermore, Fig. 23(b) presents the relationship between the thickness of the connection nodes and the reductions in yield and ultimate load capacities of the connection. The reduction in the yield and ultimate load capacities was determined relative to the reference model. As shown in the figure, reducing the thickness of the two nodes by 0–5 mm resulted in a decrease in the ultimate load capacity of the beam–column connection by 0% to 46%. Notably, an almost linear relationship was observed between the thickness of the two modular nodes and the reductions in yield and ultimate load capacities of the connection, with R-square values of 0.995 and 0.979, respectively.

6. Conclusion

The current study delves into the examination of a previously proposed S-CN cast-steel connector, utilized in combination with RHS members. The investigation is carried out through a parametric FE analysis with the primary objective of gaining an understanding of the connector's behavior under compressive loading. Additionally, the study aims to propose a method for calculating the bearing capacities of the connector by employing the existing design procedure AISC 360–16. Based on this investigation, the following findings can be drawn, however, these conclusions are limited to the scope of this study.

- The process for determining the compressive load-bearing capacity of the proposed connection is established following the guidelines and principles presented in the AISC 360–16 standard. The agreement between the experimental results of yield loads and the failure mode of the four specimens subjected to compressive load and the calculated results from AISC 360–16 was satisfactory. This offers substantiation for the reliability of both the computational and experimental results.
- FEA accurately predicted the observed failure modes in four experiments, including local buckling, crippling of node walls, and local plate crushing. The analysis also captured the initial stiffness, ultimate strength, and postpeak degrading behavior of the test specimens.
- The parametric study showed that the thickness of a tie plate has very little effect on the compressive strength of the connection. Also, the compressive load-bearing capacities of the connector and beam–column connection is affected by the thickness of the two connection nodes. It can be observed that there exists an approximately linear relationship between reducing the thickness of the wall of connection nodes and the reduction in yield and ultimate load capacity of the connection. This parametric analysis was used as the basis to select the optimal thickness of the two modular nodes, to optimize the load-bearing capability of the connection

- The mode of failure of the beam–column connection under compression loading is dependent on the relationship between the compressive capacities of the column and the connector. There may be local buckling of the nodes, local buckling of the columns and modular nodes, or totally dominant local buckling of the columns.
- If the failure mode is local buckling of the nodes, increasing the column size has limited effect on the compressive strength of the connection. The parametric study suggests that to optimize the structure's bearing capacity, the designer must choose suitable sizes for the columns, and connectors.

The study introduced an innovative modular construction approach utilizing novel cast-steel connectors and RHS members. Numerical investigations were conducted on the proposed modular floor and roof nodes, the connector, and the beam–column connection specimens. For further research, the flexural behavior and shear strength of the connection will be explored. Additionally, comprehensive experimental testing on a full-scale module's static and seismic performance is planned and will be presented in subsequent studies.

CRedit authorship contribution statement

Tran-Van Han: Conceptualization, Methodology, Formal analysis, Software, Validation, Data collection and analysis, Writing – original draft, Writing – review & editing. **Jeong MoonSook:** Writing – review & editing, Formal analysis. **YongNam Kim:** Writing – review & editing, Formal analysis. **Dongkyu Lee:** Writing – review & editing, Formal analysis. **Nguyen-Vu Luat:** Software, Validation, Data collection and analysis. **Kihak Lee:** Resources, Formal analysis, Writing – review & editing, Supervision, Project administration.

Declaration of competing interest

The authors declare that they have no known competing financial interests or personal relationships that could have appeared to influence the work reported in this paper.

Data availability

The authors do not have permission to share data.

Acknowledgments

This study was completed with financial and technical assistance of Samsung C&T Corp. located in Seoul, Republic of Korea. This research was also supported by Basic Science Research Program through the National Research Foundation of Korea (NRF) funded by the Ministry of Education (NRF-2020R1A2C2007195).

Appendix. MATLAB code for generating input for multi-linear isotropic hardening model in ANSYS

A.1. SCW550.m

```

clc; clear all
echo off;
% Creat multilinear_hardening data for SCW550 steel
%Author: Tran-Van Han
%% Based on: Paper "Proposed bilinear plus nonlinear hardening model together with
    typical experimental stress-strain curve" and ANSYS learning (https://youtu.be/
    rCFmcNWRds4?si=6Q4T6NcRsaZcTWLl)
% Unit: N, mm, MPa
% first curve
E = 205000;
sigma_y = 509; %engineering yield strength
sigma_u = 649; %engineering ultimate strength
epsilon_y = 0.17/100; % percent yield strain
epsilon_sh_formula= 0.1*(sigma_y/sigma_u)-0.055; %percent hardening strain
if epsilon_sh_formula <0.015
    epsilon_sh = 0.015;
elseif epsilon_sh_formula >0.03
    epsilon_sh = 0.03;
else
    epsilon_sh = epsilon_sh_formula;
end
epsilon_u_formula = 0.6*(1-sigma_y/sigma_u); %percent ultimate strain
if epsilon_u_formula < 0.06
    epsilon_u = 0.06;
else
    epsilon_u = epsilon_u_formula;
end
%% Draw elastic stage
n = 10; %number of data points
epsilon_elastic = linspace(0,epsilon_y,n);
sigma_elastic = E*epsilon_elastic;
epsilon_elastic = epsilon_elastic(1:end-1);
sigma_elastic = sigma_elastic(1:end-1);
figure(1)
plot(epsilon_elastic,sigma_elastic);
%% Draw yield stage
m = 6; %number of data points;
epsilon_yield = linspace(epsilon_y,epsilon_sh,m);
sigma_yield = sigma_y*ones(1,m);
epsilon_yield = epsilon_yield(1:end-1);
sigma_yield = sigma_yield(1:end-1);
figure(2)
plot(epsilon_yield,sigma_yield);
%% Draw hardening stage
k = 11; %number of data points;
epsilon_hardening = linspace(epsilon_sh,epsilon_u,k);
A = (epsilon_hardening-epsilon_sh);
B = (epsilon_u-epsilon_sh);
C = A/B;
D = (1+400*(C.^5)).^(1/5);

for i = 1:length(C)
sigma_harder = sigma_y +(sigma_u-sigma_y)*(0.4*C(i)+2*C(i)/D(i));
sigma_hardening(i,:) = sigma_harder;
end
sigma_hardening = sigma_hardening';
figure(3)
plot(epsilon_hardening,sigma_hardening);

```

```

%% Draw typical stress_strain
eng_sigma = [sigma_elastic sigma_yield sigma_hardening];
eng_epsilon = [epsilon_elastic epsilon_yield epsilon_hardening];
figure(4)
plot(eng_epsilon,eng_sigma);
title('The engineering stress-strain curve of SCW550')
xlabel('Strain (mm/mm)')
ylabel('Stress (MPa)')
%% True stress-strain
true_epsilon = log(eng_epsilon+1);
for i = 1:length(eng_sigma)
    true_sigma_cal = eng_sigma(i)*(1+eng_epsilon(i));
    true_sigma(i,:) = true_sigma_cal;
end
true_sigma = true_sigma';
figure(5)
plot(true_epsilon,true_sigma);
title('The true stress-strain curve of SCW550')
xlabel('Strain (mm/mm)')
ylabel('Stress (MPa)')
%% elastic strain
elastic_strain = true_sigma/E;
%% Plastic strain
plastic_strain = abs(true_epsilon - elastic_strain);
%% stress_strain_input
plastic_strain_input = plastic_strain(n-1:end);
plastic_stress_input = true_sigma(n-1:end);
plastic_strain_input = plastic_strain_input';
plastic_strain_input(1,1) = 0;
plastic_stress_input = plastic_stress_input';
stress_strain_input = [plastic_strain_input plastic_stress_input]; % plastic Stress-
    strain input in ANSYS
%% export data
filename = 'stress_strain_curve_input_ANSYS_SCW550.xlsx';
writematrix(stress_strain_input,filename,'Sheet',1,'Range','D1')
%
eng_epsilon = eng_epsilon';
eng_sigma = eng_sigma';
true_epsilon = true_epsilon';
true_sigma = true_sigma';

```

References

- [1] H.-T. Thai, T. Ngo, B. Uy, A review on modular construction for high-rise buildings, *Structures* 28 (2020) 1265–1290, <http://dx.doi.org/10.1016/j.istruc.2020.09.070>, Elsevier.
- [2] Z. Mortice, Can this Chicago apartment factory make new homes affordable? 2019, URL <https://www.bloomberg.com/news/articles/2019-07-08/chicago-is-getting-new-factory-made-three-flats>.
- [3] Y. Yu, Z. Chen, Rigidity of corrugated plate sidewalls and its effect on the modular structural design, *Eng. Struct.* 175 (2018) 191–200, <http://dx.doi.org/10.1016/j.engstruct.2018.08.039>.
- [4] M. Lawson, S. Popo-Ola, Modular construction using light steel framing, *New Steel Constr.* 9 (2001) 21–23.
- [5] R. Jin, J. Hong, J. Zuo, Environmental performance of off-site constructed facilities: A critical review, *Energy Build.* 207 (2020) 109567, <http://dx.doi.org/10.1016/j.enbuild.2019.109567>.
- [6] N.A. Suhaini, Investigation on Construction Waste Management At Precast Concrete Plants in Johor: Case Study (Ph.D. thesis), Universiti Tun Hussein Malaysia, 2021.
- [7] Y. Jiang, D. Zhao, D. Wang, Y. Xing, Sustainable performance of buildings through modular prefabrication in the construction phase: A comparative study, *Sustainability* 11 (2019) 5658, <http://dx.doi.org/10.3390/su11205658>.
- [8] M. Kamali, K. Hewage, Life cycle performance of modular buildings: A critical review, *Renew. Sustain. Energy Rev.* 62 (2016) 1171–1183, <http://dx.doi.org/10.1016/j.rser.2016.05.031>.
- [9] W. Ferdous, Y. Bai, T.D. Ngo, A. Manalo, P. Mendis, New advancements, challenges and opportunities of multi-storey modular buildings—A state-of-the-art review, *Eng. Struct.* 183 (2019) 883–893, <http://dx.doi.org/10.1016/j.engstruct.2019.01.061>.
- [10] J. Thompson, *Modular construction: A solution to affordable housing challenges*, 2019.
- [11] A.W. Lacey, W. Chen, H. Hao, K. Bi, Structural response of modular buildings—An overview, *J. Build. Eng.* 16 (2018) 45–56, <http://dx.doi.org/10.1016/j.job.2017.12.008>.
- [12] S. Srisangeethanan, M.J. Hashemi, P. Rajeev, E. Gad, S. Fernando, Review of performance requirements for inter-module connections in multi-story modular buildings, *J. Build. Eng.* 28 (2020) 101087, <http://dx.doi.org/10.1016/j.job.2019.101087>.
- [13] G. Nadeem, N.A. Safiee, N.A. Bakar, I. Abd Karim, N.A.M. Nasir, Connection design in modular steel construction: A review, *Structures* 33 (2021) 3239–3256, <http://dx.doi.org/10.1016/j.istruc.2021.06.060>, Elsevier.
- [14] Z. Chen, H. Li, A. Chen, Y. Yu, H. Wang, Research on pretensioned modular frame test and simulations, *Eng. Struct.* 151 (2017) 774–787, <http://dx.doi.org/10.1016/j.engstruct.2017.08.019>.
- [15] R. Sanches, O. Mercan, B. Roberts, Experimental investigations of vertical post-tensioned connection for modular steel structures, *Eng. Struct.* 175 (2018) 776–789, <http://dx.doi.org/10.1016/j.engstruct.2018.08.049>.
- [16] J. Liew, Y. Chua, Z. Dai, Steel concrete composite systems for modular construction of high-rise buildings, *Structures* 21 (2019) 135–149, <http://dx.doi.org/10.1016/j.istruc.2019.02.010>, Elsevier.
- [17] A.W. Lacey, W. Chen, H. Hao, K. Bi, F.J. Tallowin, Shear behaviour of post-tensioned inter-module connection for modular steel buildings, *J. Constr. Steel Res.* 162 (2019) 105707, <http://dx.doi.org/10.1016/j.jcsr.2019.105707>.
- [18] D. Farnsworth, *Modular building unit connection system*, 2016, US Patent 9,366, 020.
- [19] E.-F. Deng, L. Zong, Y. Ding, X.-M. Dai, N. Lou, Y. Chen, Monotonic and cyclic response of bolted connections with welded cover plate for modular

- steel construction, *Eng. Struct.* 167 (2018) 407–419, <http://dx.doi.org/10.1016/j.engstruct.2018.04.028>.
- [20] Z. Chen, J. Liu, Y. Yu, Experimental study on interior connections in modular steel buildings, *Eng. Struct.* 147 (2017a) 625–638, <http://dx.doi.org/10.1016/j.engstruct.2017.06.002>.
- [21] Z. Chen, J. Liu, Y. Yu, C. Zhou, R. Yan, Experimental study of an innovative modular steel building connection, *J. Constr. Steel Res.* 139 (2017b) 69–82, <http://dx.doi.org/10.1016/j.jcsr.2017.09.008>.
- [22] B.-H. Cho, J.-S. Lee, H. Kim, D.-J. Kim, Structural performance of a new blind-bolted frame modular beam–column connection under lateral loading, *Appl. Sci.* 9 (2019) 1929, <http://dx.doi.org/10.3390/app9091929>.
- [23] A.W. Lacey, W. Chen, H. Hao, K. Bi, New interlocking inter-module connection for modular steel buildings: Experimental and numerical studies, *Eng. Struct.* 198 (2019) 109465, <http://dx.doi.org/10.1016/j.engstruct.2019.109465>.
- [24] S. Lee, J. Park, S. Shon, C. Kang, Seismic performance evaluation of the ceiling-bracket-type modular joint with various bracket parameters, *J. Constr. Steel Res.* 150 (2018) 298–325, <http://dx.doi.org/10.1016/j.jcsr.2018.08.008>.
- [25] S.S. Lee, K.W. Bae, K.S. Park, S.Y. Hong, An experimental evaluation of structural performance for the beam to column joints in unit modular system, *J. Korean Soc. Steel Constr.* 25 (2013) 255–265, <http://dx.doi.org/10.7781/kjoss.2013.25.3.255>.
- [26] S. Sendanayake, D. Thambiratnam, N. Perera, T. Chan, S. Aghdamy, Enhancing the lateral performance of modular buildings through innovative inter-modular connections, *Structures* 29 (2021) 167–184, <http://dx.doi.org/10.1016/j.istruc.2020.10.047>, Elsevier.
- [27] S.V. Sendanayake, D.P. Thambiratnam, N. Perera, T. Chan, S. Aghdamy, Seismic mitigation of steel modular building structures through innovative inter-modular connections, *Heliyon* 5 (2019) e02751, <http://dx.doi.org/10.1016/j.heliyon.2019.e02751>.
- [28] P. Sharafi, M. Mortazavi, B. Samali, H. Ronagh, Interlocking system for enhancing the integrity of multi-storey modular buildings, *Autom. Constr.* 85 (2018) 263–272, <http://dx.doi.org/10.1016/j.autcon.2017.10.023>.
- [29] J. Dhanapal, H. Ghaednia, S. Das, J. Velocci, Structural performance of state-of-the-art vectorbloc modular connector under axial loads, *Eng. Struct.* 183 (2019) 496–509, <http://dx.doi.org/10.1016/j.engstruct.2019.01.023>.
- [30] L. Kalam, J. Dhanapal, S. Das, H. Ghaednia, Behavior of vectorbloc beam–column connections, in: *Proceedings of the Canadian Society of Civil Engineering Annual Conference 2021: CSCE21 General Track 2*, Springer, 2022, pp. 333–344.
- [31] B. Hajimohammadi, S. Das, H. Ghaednia, J. Dhanapal, Structural performance of registration pin connection in vectorbloc modular construction system, *J. Constr. Steel Res.* 197 (2022) 107464, <http://dx.doi.org/10.1016/j.jcsr.2022.107464>.
- [32] J.H. Doh, N.M. Ho, D. Miller, T. Peters, D. Carlson, P. Lai, Steel bracket connection on modular buildings, *J. Steel Struct. Constr.* 2 (2017) <http://dx.doi.org/10.4172/2472-0437.1000121>, 2472–0437.
- [33] Z. Chen, Y. Liu, X. Zhong, J. Liu, Rotational stiffness of inter-module connection in mid-rise modular steel buildings, *Eng. Struct.* 196 (2019) 109273, <http://dx.doi.org/10.1016/j.engstruct.2019.06.009>.
- [34] X.-M. Dai, L. Zong, Y. Ding, Z.-X. Li, Experimental study on seismic behavior of a novel plug-in self-lock joint for modular steel construction, *Eng. Struct.* 181 (2019) 143–164, <http://dx.doi.org/10.1016/j.engstruct.2018.11.075>.
- [35] E.-F. Deng, J.-Y. Lian, Z. Liu, G.-C. Zhang, S.-B. Wang, D.-B. Cao, Compressive behavior of a fully prefabricated liftable connection for modular steel construction, *Buildings* 12 (2022) 649, <http://dx.doi.org/10.3390/buildings12050649>.
- [36] ANSYS, *Ansys mechanical apdl element reference guide*, 2020.
- [37] P.P. Debnath, T.-M. Chan, A comprehensive numerical approach for modelling blind-bolted CFST connections, *Structures* 33 (2021) 2208–2225, <http://dx.doi.org/10.1016/j.istruc.2021.05.052>, Elsevier.
- [38] M. Fadden, J. McCormick, Cyclic quasi-static testing of hollow structural section beam members, *J. Struct. Eng.* 138 (2012) 561–570, [http://dx.doi.org/10.1061/\(ASCE\)ST.1943-541X.000005](http://dx.doi.org/10.1061/(ASCE)ST.1943-541X.000005).
- [39] Z. Chen, J. Wang, J. Liu, Z. Cong, Tensile and shear performance of rotary inter-module connection for modular steel buildings, *J. Constr. Steel Res.* 175 (2020) 106367, <http://dx.doi.org/10.1016/j.jcsr.2020.106367>.
- [40] X. Yun, L. Gardner, Stress–strain curves for hot-rolled steels, *J. Constr. Steel Res.* 133 (2017) 36–46, <http://dx.doi.org/10.1016/j.jcsr.2017.01.024>.
- [41] B. Standard, *Eurocode 3—Design of Steel Structures—, BS EN 1993-1, Vol. 1*, 2006, p. 2005.
- [42] C. EN, *1-5: Eurocode 3—Design of Steel Structures—Part 1-5: Plated Structural Elements*, CEN: Brussels, Belgium, 2006.
- [43] ANSYS, *Ansys Theory Reference*, Canonsburg, Ansys, PA, USA, 2021.
- [44] ANSYS, *Ansys Mechanical Apdl Material Reference*, ANSYS Inc, 2013.
- [45] E. 1090-2, *Execution of Steel Structures and Aluminium Structures. Part 2. Technical Requirements for Steel Structures*, 2018.
- [46] M. Seif, B. Schafer, Design of locally slender structural steel columns, *J. Struct. Eng.* 140 (2014) 04013086, [http://dx.doi.org/10.1061/\(ASCE\)ST.1943-541X.0000889](http://dx.doi.org/10.1061/(ASCE)ST.1943-541X.0000889).
- [47] A. Astm, *Standard specification for general requirements for rolled structural steel bars, plates, shapes, and sheet piling*, 2011.
- [48] S.-E. Kim, D.-H. Lee, Second-order distributed plasticity analysis of space steel frames, *Eng. Struct.* 24 (2002) 735–744, [http://dx.doi.org/10.1016/S0141-0296\(01\)00136-5](http://dx.doi.org/10.1016/S0141-0296(01)00136-5).
- [49] A. I. of Steel Construction, *Specification for Structural Steel Buildings*, AISC, 2019.
- [50] K.-H. Han, T.-S. Eom, H.-J. Hwang, J.-H. Lee, S. Kim, Behavior of hollow structural section branch-to-casting node connections for free-form grid shell structures, *J. Struct. Eng.* 148 (2022) 04022095, [http://dx.doi.org/10.1061/\(ASCE\)ST.1943-541X.0003407](http://dx.doi.org/10.1061/(ASCE)ST.1943-541X.0003407).